Ideal tensile and shear strength of a gum metal approximant: *Ab initio* density functional calculations

Naoyuki Nagasako,[1,*] Ryoji Asahi,[1,†] and Jürgen Hafner[2,‡]

[1]*Toyota Central Research and Development Laboratories Inc., Nagakute, Aichi 480-1192, Japan*

[2]*Faculty of Physics and Center for Computational Materials Science, University of Vienna, Sensengasse 8/12, AT-1090 Wien, Austria*

(Received 17 December 2011; published 31 January 2012)

The ideal tensile and shear strengths of binary β-phase Ti_3Nb alloys have been investigated using *ab initio* density functional calculations. The binary alloy is considered as an approximant to the multifunctional Ti-Nb-Ta-Zr-O alloy known as "gum metal," which displays high strength, low elastic modulus, high yield strain, and very good ductility. This alloy has been reported to deform elastically until the stress approaches the ideal tensile strength. Our calculations have been performed for an optimized chemical decoration of the body-centered cubic (bcc) structure of the β phase. Previous work has demonstrated that this model yields elastic constants in very good agreement with those measured for gum metal specimens and leads to a reasonably accurate description of the martensitic transformations between the bcc β, the orthorhombic α'' and the hexagonal ω phases [Lazar *et al.*, Phys. Rev. B **84**, 054202 (2011)]. The simulations of the response to tensile and shear loading have been performed for large supercells which account also for the different orientations of the -Nb-Nb- chains characteristic for the β-phase structure relative to the direction of the applied load. The energy-strain and stress-strain curves are found to be very different from those reported for all bcc metals. Under uniaxial ⟨100⟩ loading we find an ideal tensile strength of 2.4 GPa, the upper limit to the tensile stress arising from a shear instability of the structure. Under uniaxial ⟨110⟩ load we calculate an ideal tensile strength of 2.2 or 2.8 GPa, depending on the orientation of the -Nb-Nb- chains relative to the loading direction. For a realistic multidomain structure the ideal strength is expected to correspond to the average of these values. An ideal strength of 2.6 GPa under ⟨110⟩ loading is roughly the same as under ⟨100⟩ load, despite a considerable anisotropy of the tensile moduli. For {211}⟨111⟩ shear we calculate an ideal shear strength of 1.6 GPa, again as an average over different possible shearing directions relative to the Nb-Nb bonds. For the {110}⟨110⟩ shear system we find a lower strength of 0.9 GPa. The structures reached at the stress maximum under ⟨100⟩ uniaxial tension and {211}⟨111⟩ shear are identical, and since the maximal shear stress is much lower than the tensile stress, the alloy will fail by shear even under strictly uniaxial tension. The values of the ideal tensile and shear strengths are significantly low, even in comparison with those calculated for bcc V and Nb with very small shear moduli and approach the values reported for gum metal alloys.

DOI: 10.1103/PhysRevB.85.024122 PACS number(s): 62.20.F−, 62.25.−g, 81.40.Jj

I. INTRODUCTION

The phase stability of Ti alloys can be changed by adding alloying elements such as vanadium,[1] niobium,[2,3] molybdenum,[4] or tantalum,[5] which stabilize the body-centered cubic (bcc) β phase at ambient or elevated temperatures. The limit of bcc stability is determined by the vanishing of the elastic shear modulus $C' = (C_{11} - C_{12})/2$ and correlated to a critical electron-per-atom ratio of $e/a \sim 4.15$ (Refs. 6 and 7). The stabilization of the β phase is of practical importance because it enhances deformation capability and strength of the alloy.

The name gum metal has been given to a class of Ti-Nb-Ta-Zr-O alloys developed at the Toyota Central R&D Laboratories which display high strength, a low elastic modulus, high yield strain, and a very good ductility.[8] These properties are achieved by adjusting the alloy composition such that the average electron-per-atom ratio comes close to a critical value of $e/a \sim 4.24$ for which *ab initio* calculations of the elastic constants of binary Ti-based alloys have predicted a vanishing tetragonal shear constant.[9] In addition, the alloy requires cold working. Under tensile loading the material deforms elastically until the stress approaches a value assumed to come close to the ideal tensile strength.[10–12] An ideal tensile strength of $\sigma_{max} \sim 1.5$ GPa has been estimated using the semiempirical relation $\sigma_{max} = 0.08 \times E_{100}$ where $E_{100} = 19$ GPa is the modulus for tension along [100] calculated from the predicted elastic constants.[9] This relation between tensile strength and tensile modulus is based on the assumption of a sinusoidal stress-strain curve and a deformation following the tetragonal Bain path with a face-centered cubic saddle-point structure and is known to hold for many, but not all bcc metals.[13–15] After yield strong plastic deformation occurs with little evidence for dislocation glide. Rather, deformation proceeds via the formation of extended shear bands referred to as "giant faults" at an applied stress close to the ideal shear strength.[11,16,17] The condition for failure by shear under strict tensile loading is that the shear strength is significantly lower than the tensile strength. An ideal shear strength of $\tau_{max} \sim 0.9$ GPa has been estimated using the empirical relation $\tau_{max} = 0.11 \times G_{111}$ and a calculated value of the shear modulus of $G_{111} = 12$ GPa (Ref. 9) (but again with the caveat that this empirical relation is based on the assumption of a sinusoidal stress-strain curve and does not necessarily hold for all bcc metals and alloys[13–15]). A dislocation-free mechanism of deformation has been described by Kiritani *et al.* for thin foils of face-centered cubic (fcc)[18] and bcc[19] metals, but for polycrystalline coarse-grained or single-crystalline materials plastic deformation without dislocation glide seems to be unique for gum metal.

The response of gum metal specimens (composition Ti-23Nb-0.7Ta-2Zr-1.2O in at.%) to tensile loading has been the subject of several experimental studies. Takesue *et al.* performed tensile tests along the ⟨100⟩, ⟨110⟩, and ⟨111⟩ directions on single-crystal samples. At the lowest oxygen content of 0.3 to 0.5 mass % a tensile strength of 0.5–0.6 GPa was reported for all three loading directions, the strength increases to up to 1.0 GPa at increased oxygen content. Crystals loaded in tension along ⟨100⟩ and ⟨111⟩ showed linear stress-strain relations up to yield, but loading along ⟨110⟩ displayed a sharp "pseudoyield" at a strain of only 0.5%, followed by an extensive "pseudoelastic deformation" before undergoing plastic yield. Recently, very similar results have been reported by Morris *et al.*[20] It was demonstrated that while uniaxial tensile strain along ⟨110⟩ promotes a stress-induced transformation from the β (bcc) to the α'' (orthorhombic) phase stable at low temperatures,[21] crystals grown and strained in the ⟨100⟩ or ⟨111⟩ directions did not transform at all. The initial slopes of the stress-strain curves also permitted an estimate of the tensile moduli and it was pointed out that the measured yield strength was only about half the value of the ideal strengths estimated for the moduli, using the empirical relations.[20] The deformation of single-grain nanopillars of Gum Metal under compression has been investigated by Withey *et al.*[22] Under compression a crystal fails if the resolved stress for the {110}⟨111⟩, {112}⟨111⟩, or {123}⟨111⟩ slip systems reaches the critical value. Depending on the processing conditions of the samples an average value of the shear strength of $\tau_{\max} = 0.85$ GPa was reported, the highest values reaching 1.4 to 1.7 GPa. These values come very close to the ideal shear strength estimated from the calculated elastic constants. Martensitic transformations to the α'' phase were observed in some, but not in all samples. Yang *et al.*[23] investigated alloys of similar composition (Ti-22.4Nb-0.73Ta-2.0Zr-1.34O) under compression and tension. The samples showed linear elasticity up to strains of about 2.3% at a low tensile modulus of 55 GPa and a strongly temperature-dependent tensile strength, decreasing from ∼1.8 GPa at $T = -200\,^{\circ}$C to ∼1.0 GPa at room temperature. The influence of the oxygen content on the properties of gum metal alloys was studied very recently by Besse *et al.*[24] The tensile curve of the alloys without oxygen shows the double yielding behavior observed in many β-phase Ti alloys, with a pseudoyield stress of about 0.2 GPa, followed by a plateau with slowly increasing stress up to a tensile strength of 0.4 GPa. The alloys containing oxygen showed a yield strength of 0.83 GPa, the ultimate tensile strength of 0.88 GPa being only slightly higher. It was concluded that the difference in the mechanical behavior results from the suppression of the formation of α'' martensite by the addition of oxygen.

Hence, one of the central problems in the characterization of the intrinsic properties of Ti alloys related to gum metal is the determination of the ideal tensile and shear strengths which have so far only been estimated from the elastic moduli, using semiempirical relations. The elastic properties and the ideal strength can, in principle, be determined with good accuracy from *ab initio* density-functional calculations. However, due to the complexity of the alloys such calculations have been performed so far only using the most rudimentary models. The calculations of the elastic constants of binary Ti- and Zr-based alloys of Ikehata *et al.*[9] are based on the assumption that at a stoichiometry of A_3B the alloy forms an ordered $D0_3$-type structure, while for the AB alloys a B2 structure was assumed. Li *et al.* calculated the elastic moduli and the ideal tensile and shear strength of bcc Ti-V alloys in a virtual-crystal approximation (VCA).[25] Within the VCA a binary alloy is described as an effective one-component system consisting of atoms with the concentration-averaged pseudopotentials of the elements composing the alloy. Because the concentration-averaged pseudopotential can be calculated only for elements with the same ionic core, instead of gum metal consisting mainly of Ti ($3d$) and Nb ($4d$) the calculations have been performed for Ti-V alloys where both constituents are $3d$ metals. Nevertheless, the analysis produces some interesting results. (i) Two tensile (E_{100}, E_{110}) and two shear moduli (G_{110}, G_{111}) vanish almost simultaneously at an electron-per-atom ratio of $e/a \sim 4.1$, indicating the incipient instability of the bcc crystal structure. (ii) The ideal shear strength $\tau_{\max} \sim 1.2$ GPa derived from the stress-strain curve calculated for simple shear along (112)[111] conforms rather well with the shear modulus and the semiempirical relation based on a transformation to a stress-free body-centered-tetragonal state. (iii) Similarly, an ideal tensile strength of $\sigma_{\max} \sim 1.8$ GPa conforms rather well with the calculated tensile modulus and a transformation along a tetragonal Bain path. This last result is a bit surprising because it has been demonstrated[15] that for bcc V and Nb a bifurcation from the primary tetragonal deformation path (PTP, the Bain path) to a secondary orthorhombic deformation path (SOP) occurs before reaching the stress maximum. The saddle-point structure along the SOP is a "special bct" structure which is identical to the saddle-point structure under shear deformation along a {111} plane. For bcc Ta and Mo the stress maxima along the PTP and the SOP coincide. Because the stress maximum under tensile loading is reached at a shear unstable configuration the metals fail by shear even under tensile loading (as found also for the gum metal alloys). V-rich VCA Ti-V alloys show the same behavior as V metal, but for alloys with less than 45 at.% V the bifurcation to the SOP occurs only at strain larger than corresponding to the stress-maximum on the PTP. Hence, a $Ti_{75}V_{25}$ alloy is predicted to fail in tension and not by shear, in contrast to gum metal alloys. Li *et al.*[25] have argued, with reference to the calculations of the elastic constants by Ikehata *et al.*[9] that Ti-Nb alloys will behave differently from Ti-V alloys because of a lower value of the C_{44} shear constant. Indeed $C_{44} = 0$ (in a bct reference frame) is the necessary condition for the bifurcation from the PTP to the SOP under uniaxial loading along ⟨100⟩. However, a lower value of the shear constant at vanishing strain does not necessarily imply that it will be reduced to zero at increasing strain.

Investigations of ordered intermetallic compounds have demonstrated that only for a strictly random substitutional alloy consisting of two very similar elements is it legitimate to expect that the deformation under large strains follows the same scenario as for pure metals with the same crystal symmetry. For the B2(CsCl)-type aluminides of Fe, Co, and Ni it has been demonstrated[26–28] that under uniaxial tension along ⟨111⟩ the crystal follows a trigonal deformation path and the structure finally becomes B1(NaCl) at a strain of ∼0.68.

By symmetry, the B1 structure is stress free; it corresponds to an energy-maximum along the deformation path. Under these circumstances, the theoretical strength of bcc B2-type intermetallic compounds under ⟨111⟩ tension is determined by an fcc (B1) saddle-point structure, as for most metals. However, the situation is entirely different for uniaxial tension along ⟨100⟩ or ⟨110⟩. Under ⟨110⟩ loading a B2 crystal follows a monoclinic deformation path along which no other high-symmetry or stress-free structure is encountered. Under ⟨100⟩ tension the crystal follows a tetragonal deformation path leading to a transformation to a $L1_0$ (CuAu) structure. Since the $L1_0$ structure has reduced symmetry compared to B2 it is not stress free. Also, no other high-symmetry structure is found along the deformation path. Hence, under ⟨100⟩ and ⟨110⟩ tension the theoretical strength of B2-type compounds is not symmetry-dictated as for bcc metals along the Bain path for the bcc → fcc transformation under ⟨100⟩ tension. In addition, the calculations[28] have demonstrated that unlike for NiAl and CoAl, where ⟨100⟩ is the hard direction under uniaxial tension, for FeAl a local stress maximum is found at relatively low strain. Although this stress maximum is much lower than the global maximum (which is of comparable magnitude for all three aluminides), it determines the theoretical tensile strength of FeAl. Li *et al.*[28] have also investigated the response of the three B2-type compounds to {112}⟨111⟩ and {110}⟨111⟩ shear loading. It was demonstrated that the B2 crystals do not have the bct saddle-point structure characteristic for the shear deformation paths of the bcc metals. Again the energy-strain and stress-strain curves of NiAl and FeAl were found to be very different, leading to the conclusion that the instabilities under ⟨111⟩ shearing and ⟨100⟩ tension can be attributed to the same mechanism for FeAl, but not for NiAl. Jahnatek *et al.*[29,30] have demonstrated that the chemical decoration of the fcc lattice in $L1_2$ and $D0_{22}$-type trialuminides of Sc, Ti, and V determines similarities and differences in the response to ⟨110⟩ and ⟨100⟩ uniaxial loading compared to fcc Al.

Hence, the chemical decoration of the bcc lattice is of decisive importance in determining the mechanical properties of β-type Ti-based alloys. Originally, the intention of the present work was to extend the work of Ikehata *et al.*[9] on the elastic properties of binary gum metal approximants to a calculation of their ideal shear and tensile strengths. However, difficulties arose already at a lower level. New calculations of the elastic constants of $D0_3$-type Ti-(V, Nb, Ta) alloys with

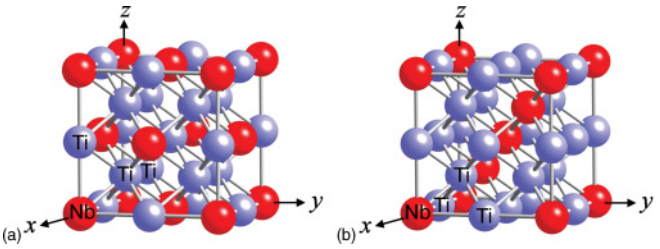

FIG. 1. (Color online) Comparison of the $D0_3$ (a) and G1 (b) structures for a Ti_3Nb alloy. The atomic positions within the irreducible rhombohedral unit cell are labeled with the chemical symbols of the constituents. Ti atoms are shown in blue (light gray), Nb atoms in red (dark gray) (cf. text).

improved all-electron methods found Ti_3V and Ti_3Nb to be elastically unstable (negative values of C_{44}), calculations of formation energies for point defects also produced negative values for antisite defects in Ti_3Nb if a full relaxation in a large supercell was permitted.[31] Hence, the assumption that an ordered $D0_3$ structure provides a realistic model for the structure of the alloy turned out to be invalid, leading to the necessity to construct a better structural model. Very recently, Lazar *et al.*[31] have presented detailed investigations of the stability and phase transitions of β-, α'-, α''-, and ω-type Ti_3Nb alloys. The optimal configuration of the β-phase was derived from supercell calculations comparing the energies of all possible chemical decorations of a large 16-atom cell, as well as by cluster-expansion calculations. Both approaches lead to the same optimal decoration of the bcc lattice called the G1 structure. In contrast to the $D0_3$ structure where each Nb atom is coordinated by Ti only, in the G1 structure the Nb atoms occupy the sites along the body diagonal of a $2 \times 2 \times 2$ bcc supercell with direct Nb-Nb neighbors (see Fig. 1). It should be noted that the structure shown in the figure is only one of 16 symmetry-equivalent decorations of the supercell.[31]

For the G1 structure *ab initio* calculations yield elastic constants in agreement with experiments on gum metal alloys.[32–34] Because of their importance for the following discussions the results, together with the tensile and shear moduli for the principal symmetry directions, are summarized in Table I. If the empirical relations between the elastic moduli and the ideal strengths are used, we calculate an ideal tensile strength of $\sigma_{\max}^{100} = 4.3$ (4.0) GPa and an ideal shear strength

TABLE I. Elastic constants and tensile and shear moduli (in GPa) calculated for bcc G1-type Ti_3Nb alloys, compared with experimental results measured on gum metal specimens of slightly different compositions (cf. text).

Alloy	C_{11}	C_{12}	C_{44}	C'	E_{100}	E_{110}	E_{111}	G_{100}	G_{110}	G_{111}	Reference
Ti_3Nb (G1)	148.8	111.4	37.5	18.7	53.4	83.2	101.8	37.5	18.7	22.4	31
Ti-23Nb-0.7Ta-2Zr-O[a]			28.5–36.6	12.3–17.8	40.0				12.3–13.7	15.1	32
Ti-33Nb-0.7Ta-2Zr-O[a]											
EP[b]	125	93	28	16	49.7	71.8			16	18.7	33
HP[c]	125	90	31	17.5	45.7	65.8			17.5	20.5	33

[a]Composition given in at.% (cf. text).
[b]Produced from elemental powders and cold pressing.
[c]Produced by plasma spraying and hot pressing.

of $\tau_{\max}^{111} = 2.5$ (2.3) GPa from the theoretical (experimental) elastic constants.

Calculations of the phonon dispersion relations for the G1 structure have shown that in the harmonic approximation the G1 structure is dynamically unstable, with imaginary optical phonon modes extending over most of the Brillouin zone. However, the G1 structure is stabilized already at temperatures around 200 K by anharmonic phonon-phonon interaction (treated in a self-consistent phonon approximation[35,36]), in contrast to the $D0_3$ structure where imaginary phonon modes were found to persist even at very high temperature.[31]

Hence, the choice of an appropriate chemical decoration of the basic bcc lattice is essential for achieving a dynamical stability of the β phase at elevated temperatures.[31] Three kinds of phase transformations ($\beta \rightarrow \alpha', \alpha'', \omega$) have been reported for β-Ti-based alloys. α' martensite is hexagonal as the α phase of pure Ti, α'' martensite is orthorhombic, and the ω phase is hexagonal. The α'' and ω phases can be formed from the β phase by cooling or isothermal aging at intermediate temperatures. A $\beta \rightarrow \alpha''$ transformation can also be induced by applying uniaxial strain. While a $D0_3$-type superstructure of the bcc lattice (and many other possible chemical decorations) lead to an elastic instability and soft optical and acoustic modes which cannot be stabilized by anharmonic phonon-phonon interactions, the optimized G1 structure is stable against shear deformations and the soft optical modes are stabilized already at moderate temperature. The necessity to create an ordered distribution of the Ti and Nb atoms on the bcc lattice has also significant consequences for the phase transformations. Both the orthorhombic α'' and the hexagonal ω structures can be created by a continuous deformation of the bcc lattice. However, whereas the deformation of the G1 structure leads to a stable ω structure, the transition to the α'' structure also has to involve a change in the chemical decoration—which is possible at elevated temperature, but not in quenched samples. This provides a rationale for the observed competition between the formation of ω and α'' precipitates.

In the present work we have used the G1 model structure for the β-type Ti_3Nb alloy to calculate the ideal tensile and shear strengths of this gum metal approximant using first-principles density functional techniques. Our paper is organized as follows: Section II describes the computational setup, Sec. III describes the structural model for the β-phase, and Secs. IV and V report our results for the ideal tensile and shear strength for loading along different symmetry directions. We summarize in Sec. VI.

II. COMPUTATIONAL METHODS

Our *ab initio* total-energy and force calculations are based on density-functional theory (DFT) as implemented in the Vienna *ab initio* simulation package (VASP).[37,38] A gradient-corrected functional has been used to describe electronic exchange and correlations.[39] Electron-ion interactions are treated within the projector-augmented-wave (PAW) method.[40,41] The plane-wave basis set contained components with kinetic energies up to 350 eV.

The response of the crystal to tensile or shear deformations was calculated by increasing the strain along the chosen directions in small steps. A quasireversible deformation process at zero absolute temperature was considered. The crystal structure was fully relaxed at each deformation step until all lateral stresses vanished. This has been done by very efficient external optimizer GADGET developed by Bučko *et al.*[42] GADGET performs a relaxation in terms of generalized coordinates which allow a better control of lateral stresses. The forces acting on the atoms were computed via the Hellmann-Feynman theorem,[43] the stress tensor acting on the unit cell was computed via the generalized virial theorem.[44] The use of a high cutoff energy makes it possible to achieve a high accuracy of the components of the stress tensor.

The energy-strain and stress-strain curves were calculated for large supercells adapted to the guiding symmetry along the deformation path. The Brillouin zone (BZ) was sampled using various types of meshes according to the size and symmetry of the computational cells. Very fine k-point meshes are required to calculate the elastic shear constants and the stress-strain relations (details are given below together with the information on the supercells used for the simulations). All integration meshes were constructed according to the Monkhorst-Pack scheme.[45] The integration over the BZ used the Hermite-Gaussian smearing method with a smearing parameter of 0.2 eV.[46] The total energy was calculated with high precision, converged to 10^{-8} eV/atom. The structural relaxation was stopped when all forces acting on the atoms were converged to within 10^{-3} eV/Å and all components of the stress tensor except that conjugate to the imposed strain were converged to within 0.05 GPa.

III. STRUCTURE MODEL FOR THE β PHASE OF Ti_3NB ALLOYS

The energetically most favorable chemical decoration of a bcc supercell with 16 atoms is achieved by the G1 structure. This structure has space-group symmetry $R\bar{3}m$ with a lattice constant of $a_0 = 6.524$ Å of the cubic unit cell containing 16 atoms. A schematic representation of the unit cell is shown in Fig. 1, where it is confronted with the $D0_3$ structure. The essential difference between the two alloy models is evident: Whereas in the $D0_3$ lattice each minority atom has only majority atoms in the first coordination shell, in the G1 structure the minority atoms are arranged along the room-diagonal of the unit cell. Similar arrangements of nearest-neighbor Nb-Nb bonds in zig-zag or spiral chain form are also characteristic for other low-energy structures, emphasizing the importance of strong Nb-Nb interactions for the structural stability.[31] Like for the $D0_3$ structure, the G1 structure may also be described by a smaller rhombohedral unit cell with only four atoms. In Fig. 1 the atomic positions in the irreducible unit cell of both structures are labeled with the chemical symbols of the constituents.

Alternatively, the G1 structure may also be represented by a face-centered monoclinic unit cell (space group $C2/m$, No. 12) with eight atoms. This may be achieved in three different ways. The b direction of the monoclinic cell is always along a face diagonal of the large cubic cell, the c direction along the body diagonal; different orientations may be chosen for the a direction. Therefore, the lattice constants are $b = a_0 \times \sqrt{2} = 9.222$ Å and $c = a_0 \times \sqrt{3}/4 = 2.828$ Å for all three variants. In the case of MC1 the a direction is along another body

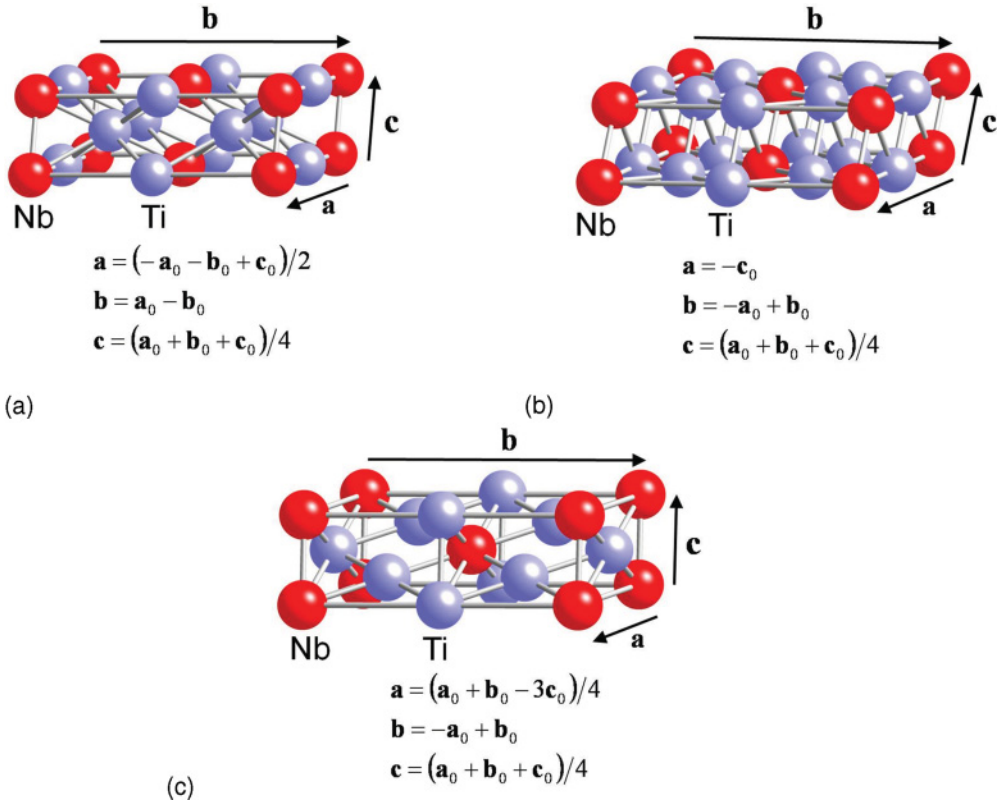

FIG. 2. (Color online) Possible face-centered monoclinic unit cells for the G1 structure of a Ti_3Nb alloy: MC1 (a), MC2 (b), and MC3 (c). The vectors $\boldsymbol{a}_0$, $\boldsymbol{b}_0$, and $\boldsymbol{c}_0$ indicate the primitive lattice vectors of the G1 structure, respectively (cf. text).

diagonal, $a = a_o \times \sqrt{3}/2 = 5.648$ Å, $\beta = 109.5°$. For variant MC2, the a direction is along one of the cube edges, $a = a_0$, $\beta = 125.3°$. Finally, in the case of MC3 the a direction is along the $[11\bar{3}]$ direction, $a = a_0 \times \sqrt{11}/4 = 5.407$ Å, $\beta = 100.0°$. All three monoclinic cells are shown in Fig. 2. The monoclinic representations have been found to be very helpful for the identification of the guiding symmetry under tensile or shear loading and of the structures at the stress maxima.

In the following, the G1 structure has been used to compute the ideal tensile and shear strengths of β-phase Ti_3Nb alloys at zero temperature. However, this does not mean that we claim that the β phase is an ordered intermetallic compound. First, the G1 structure is only one among 16 symmetry-equivalent and energetically degenerate configurations with the same 16-atom bcc supercell.[31] A real alloy will consist of a disordered arrangement of domains consisting of these 16 configurations. Second, the energy differences between the various ordered structures are sufficiently small such that low-energy configurations can be realized at a local level, the increase in internal energy being compensated by a gain in configurational entropy. One should also not forget that at low temperatures the β phase is only metastable. Indeed, a similar analysis has shown that lower total energies can be achieved for hexagonal structures and for orthorhombic lattices related to the structure of the α'' phase. Calculations of the martensitic transition temperature, using the G1 model structure, have shown that the β phase is stable above about 700 K and transforms to the orthorhombic α'' phase below. Below 200 K the hexagonal ω phase also has a lower energy than the G1 structure. Above 200 K the G1 structure is dynamically at least metastable; below this temperature imaginary optical phonons appear, but the structure remains stable against elastic deformations.

Hence, in the discussion of the simulations of tensile and shear loading one has to remember the following. (i) The G1 structure is only metastable. Although it is elastically stable at zero strain, imaginary phonon modes exist and shear instabilities may appear at finite strain. (ii) For a multidomain phase consisting of symmetry-equivalent realizations of the G1 structure simulations of tensile and shear deformations along directions equivalent under bcc symmetry yield identical results. However, this is not necessarily so for cells consisting of a single variant of the G1-type configurations. For tensile loading along a ⟨100⟩ direction strains applied in the [100], [010], or the [001] direction act in the same way on the Nb-Nb chains oriented along a ⟨111⟩ direction. However, for strains along a ⟨110⟩ direction this is not the case, because the (110) plane containing the Nb-Nb chains characteristic for the G1 structure can be either parallel or perpendicular to the direction of loading. The differences arising from the different orientations of the Nb-Nb chains relative to the direction of the applied load have been considered by using different supercells, as described in detail below.

IV. RESPONSE TO UNIAXIAL TENSILE LOADING

A. [100] uniaxial loading

Uniaxial tension along ⟨100⟩ transforms the bcc to the fcc crystal structure along the tetragonal "Bain path" (the primary

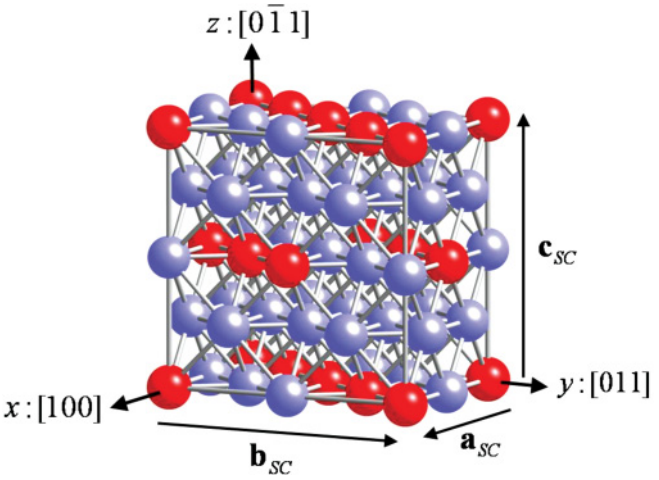

FIG. 3. (Color online) Supercell used for calculating the energy-strain and stress-strain relations of G1-type Ti_3Nb to [100] tensile loading along an orthorhombic deformation path.

tetragonal path, PTP). As shown by Hill and Milstein,[47] a branching from the PTP to a secondary orthorhombic deformation path (SOP) can occur at a "special invariant state" characterized by $C_{44} = 0$ in a body-centered tetragonal (bct) reference frame. The bct saddle-point structure along the SOP is isostructural to the metastable bct structure reached along the PTP via the fcc saddle-point structure. Among the bcc metals, a bifurcation to an SOP has been found for V and Nb, limiting the yield strain and the ideal tensile strength to $\epsilon_c^{100} = 0.10(0.11)$ and $\sigma_{\max}^{100}/E_{100} = 0.07(0.09)$ for V(Nb).[15] The bct saddle-point configuration reached on the SOP under uniaxial ⟨100⟩ loading is identical to that reached under shear along a ⟨111⟩ axis. Hence, V and Nb fail by shear even under purely uniaxial ⟨100⟩ loading. Ta is a special case, because the bifurcation to the SOP coincides with the stress maximum along the PTP; hence, Ta will also fail by shear.

To investigate the behavior of a Ti_3Nb alloy under [100] tensile strain we have used two different supercells: (i) the cubic unit cell of the G1 structure shown in Fig. 1 with tension applied along one of the cube edges, and (ii) a doubled orthorhombic supercell containing 32 atoms, rotated by 45° such that the -Nb-Nb- chains are directed along one of the face diagonals, in a plane containing the direction of the applied tensile load (see Fig. 3). Brillouin-zone integrations have been performed using a $8 \times 8 \times 8$ mesh for the tetragonally deformed cell and a $5 \times 4 \times 4$ mesh for the orthorhombic cell. We have carefully verified that this is largely sufficient for achieving k-point convergence. The lattice parameters and k-point meshes for all supercells used in our simulations are summarized in Table II.

1. Simulations using the cubic unit cell

Figures 4(a) and 4(b) show the energy-strain and stress-strain curves under uniaxial loading along [100], calculated using the cubic unit cell of G1-type Ti_3Nb. We compare the results of two different simulations differing in the guiding symmetry and in the strain increment added at each new step of the simulation. In case 1 the applied uniaxial tensile strain reduces the symmetry of the computational cell to tetragonal. From the initial slope of the stress-strain curve we derive a tensile modulus of $E_{100} = 53.64$ GPa, in excellent agreement with the value of 53.4 GPa derived from the elastic constants. A stress maximum is reached along this tetragonal deformation path at a critical strain of $\epsilon_c^{100} = 0.08$, resulting in an ideal tensile strength (ITS) of $\sigma_{\max}^{100} = 2.45$ GPa. Beyond the stress maximum the system continues along the tetragonal deformation path up to a strain of $\epsilon = 0.1$ where a monoclinic deformation in the plane perpendicular to the applied load sets in [see Fig. 4(c)].

The dimensionless ITS is $\sigma_{\max}^{100}/E_{100} = 0.046$. Both the critical strain and the dimensionless ITS are much lower than the values characteristic for tensile deformation of bcc metals along the tetragonal Bain path. For bcc V and Nb (which both have a very low value of E_{100}), the dimensionless ITS is about 0.11 to 0.12, for the "normal" bcc metals Mo and W a lower value of 0.07 to 0.08 has been calculated. The low value of the ITS found for the gum metal approximant is associated with an asymmetric stress-strain curve differing from that of any of the bcc metals.

In case 2 the symmetry of the computational cell is initially broken such that $b_{\mathrm{SC}} \neq c_{\mathrm{SC}}$, facilitating a tensile deformation along an orthorhombic deformation path. In addition, the strain has been carefully increased by smaller increments. For strains up to $\epsilon \sim 0.06$ both simulations produce identical results. An orthorhombic shear instability appears at a strain of $\epsilon = 0.06$, just before reaching the stress maximum along the tetragonal deformation path. The instability limits the ITS along ⟨100⟩ to 2.4 GPa. The energy-strain curve shows only a slight inflection, but the stress collapses to a lower value. In the plane perpendicular to the applied load, the structure is tetragonally distorted, $b_{\mathrm{sc}} \neq c_{\mathrm{sc}}$. Under further increased load, the orthorhombic distortion decreases again until at a strain of $\epsilon = 0.17$ it disappears completely. At already slightly lower strain, a monoclinic deformation in the (100) plane appears [see Fig. 4(d)].

TABLE II. Supercells used for the simulations of the response to tensile loading (cf. text).

	Tensile loading			
	[100] (Type 1)	[100] (Type 2)	[110] (Type 1)	[110] (Type 2)
x axis	$[100], a_0 = 6.524$ Å	$[100], a_{\mathrm{SC}} = a_0$	$[110], a_{\mathrm{SC}} = \sqrt{2} \times a_0$	$[1\bar{1}0], a_{\mathrm{SC}} = \sqrt{2} \times a_0$
y axis	$[010], b = a_0$	$[011], b_{\mathrm{SC}} = \sqrt{2} \times a_0$	$[\bar{1}10], b_{\mathrm{SC}} = \sqrt{2} \times a_0$	$[110], b_{\mathrm{SC}} = \sqrt{2} \times a_0$
z axis	$[001], c = a_0$	$[0\bar{1}1], c_{\mathrm{SC}} = \sqrt{2} \times a_0$	$[001], c_{\mathrm{SC}} = a_0$	$[001], c_{\mathrm{SC}} = a_0$
N_{atoms}	16	32	32	32
k mesh	$8 \times 8 \times 8$	$5 \times 4 \times 4$	$5 \times 5 \times 7$	$5 \times 5 \times 7$

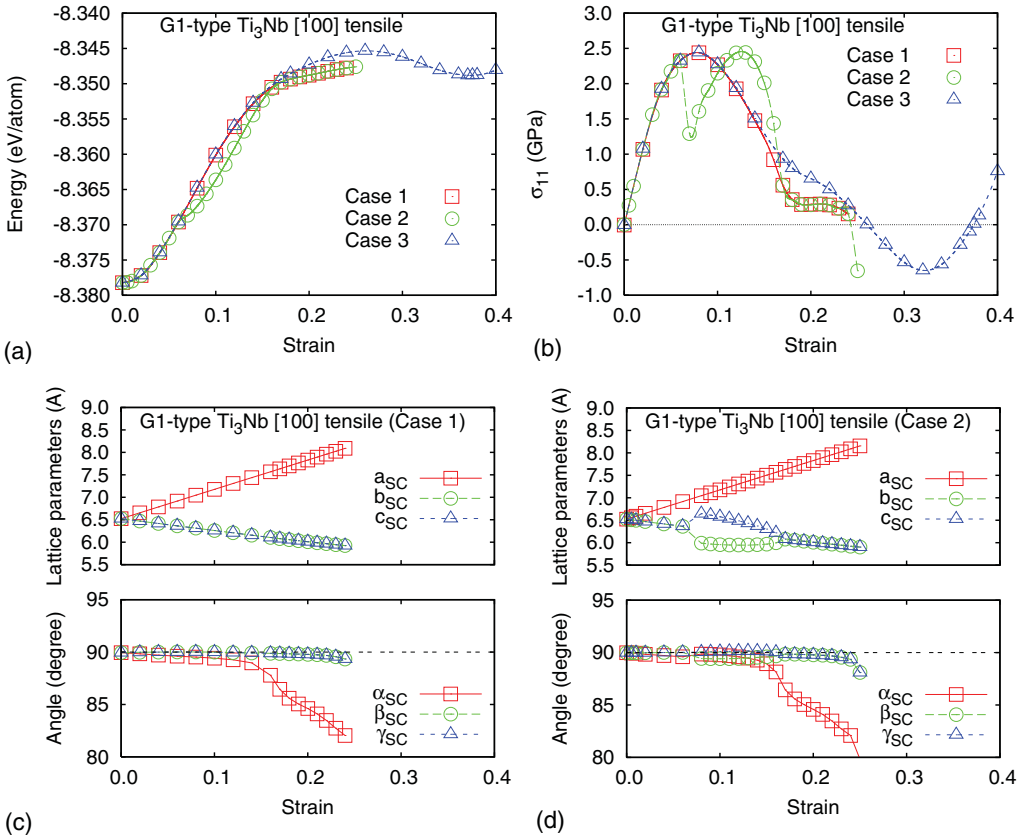

FIG. 4. (Color online) Variation of the total energy (a), the stress (b), and the lattice constants (c),(d) of G1-type Ti_3Nb under [100] tension as a function of the applied strain, calculated using the cubic unit cell of the G1 structure. The two simulations shown in the diagram (case 1 and case 2) differ by a shear instability at a strain of $\epsilon_{11} = 0.06$, just before reaching the stress maximum, in case 2. In case 3, calculations are performed with the angle α_{SC} of the supercell fixed at 90° (cf. text).

The instabilities along the tetragonal deformation path are correlated to the variation of the elastic constants of the tetragonal structure under increasing strain. The conditions for the stability of the tetragonal structure are that the subdeterminants of the elastic tensor are all positive; that is,

$$C_{11} > 0, \tag{1}$$

$$C_{11} \cdot C_{22} - C_{12}^2 > 0, \tag{2}$$

$$C_{11} \cdot \left(C_{22}^2 - C_{23}^2\right) + 2C_{12}^2 \cdot (C_{23} - C_{22}) > 0, \tag{3}$$

$$C_{44} > 0. \tag{4}$$

Figure 5 shows the variation of the elastic constants of body-centered tetragonal Ti_3Nb under uniaxial strain along the [100] direction. At a strain of $\epsilon = 0.06$ we find $C_{11} = C_{12}$ and $C_{22} = C_{23}$, violating condition (3). The tetragonal structure becomes unstable against an orthorhombic deformation, as observed in case (2). It must be emphasized, however, that the instability differs from that observed for uniaxially strained bcc metals at the bifurcation to an orthorhombic deformation path, which is driven by the vanishing of the shear constant C_{44}.[15] For the Ti_3Nb alloy C_{44} vanishes only at a much larger strain of $\epsilon \sim 0.18$. At a strain of $\epsilon = 0.1$ we find $C_{12} = C_{22}$, coincident with the instability of the tetragonal structure against monoclinic shear found in case (1). The comparison of the two simulations shows that for a system with a rather flat energy landscape weak instabilities are easily bypassed if the strain is increased by too-large increments. At a given strain the energies calculated for case 1 and case 2 differ by more than 3 meV/atom.

The structure at the stress maximum along the tetragonal deformation path at $\epsilon = 0.08$ is best described as a deformation

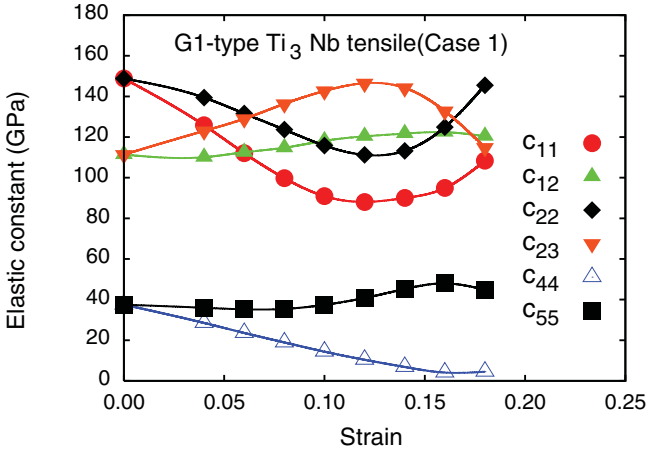

FIG. 5. (Color online) Variation of the elastic constants C_{11}, C_{12}, C_{22}, C_{23}, C_{44}, and C_{55} (related to a body-centered tetragonal lattice) of G1-type Ti_3Nb along the tetragonal deformation path as a function of uniaxial [100] strain. The elastic constants reduce to C_{11}, C_{12}, and C_{44} in the bcc limit.

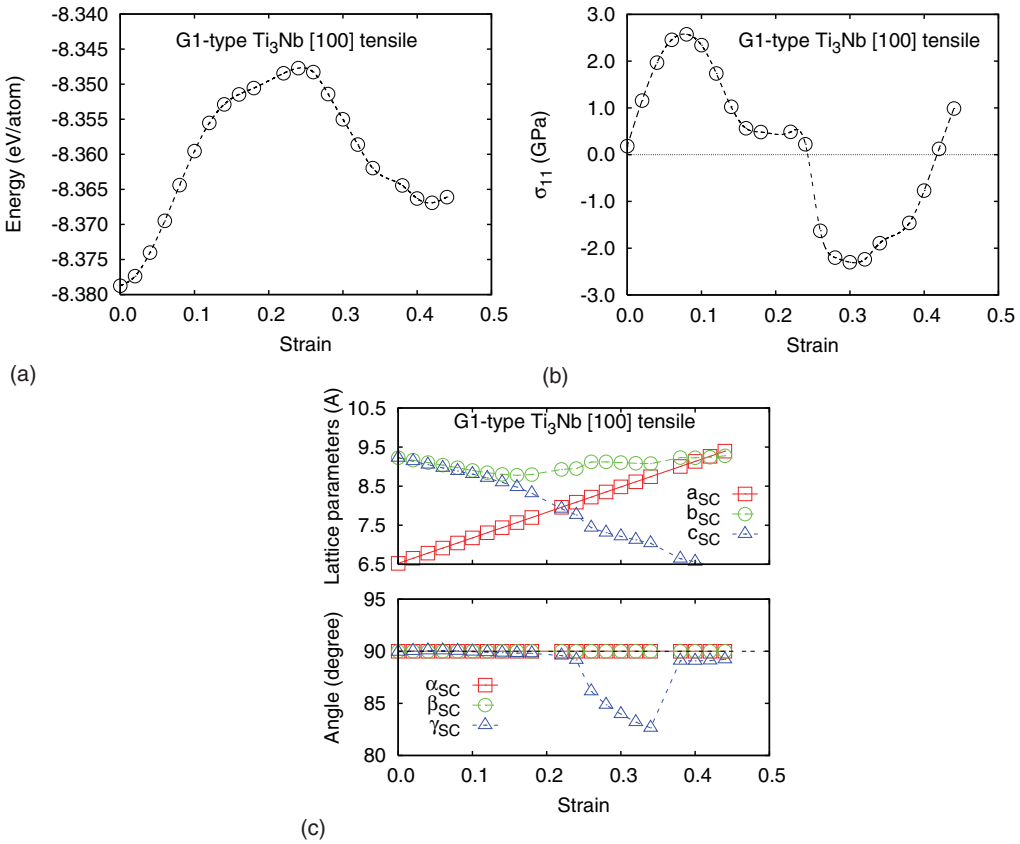

FIG. 6. (Color online) Variation of the total energy (a), the stress (b), and the lattice constants (c) of G1-type Ti_3Nb under [100] tension as a function of the applied strain, calculated for the doubled, rotated supercell shown in Fig. 3 (cf. text).

of the monoclinic unit cell MC1, with lattice constants $a = 5.70$ Å, $b = 8.89$ Å, $c = 2.85$ Å, and $\beta = 103.66°$. This structure differs only slightly from that at $\epsilon = 0.06$, where the bifurcation to an orthorhombic structure has been found in case (2), with $a = 5.69$ Å, $b = 8.98$ Å, $c = 2.84$ Å, and $\beta = 105.1°$.

At larger strains, no stress-free high-symmetry structure could be identified. Between $\epsilon = 0.20$ and $\epsilon = 0.24$ the stress is reduced to very low values. At this point the monoclinic lattice parameters are $a = 5.98$ Å, $b = 7.77$ Å, $c = 3.04$ Å, and $\beta = 95.7°$. To investigate whether the stress maximum along the tetragonal path could be related to a high-symmetry saddle-point structure which has been bypassed in the other simulations because of the monoclinic shear distortion, we have performed a third run with the angle α_{SC} of the supercell fixed at 90°. The results are included in Fig. 4 as case (3). In this case the energy-strain curve has a maximum at $\epsilon = 0.26$ at an energy which is 32.8 meV/atom higher than the G1 structure, followed by a flat energy minimum at $\epsilon = 0.375$. Within the monoclinic lattice, the stress-free structure has lattice constants $a = 5.83$ Å, $b = 8.29$ Å, $c = 2.93$ Å, and $\beta = 90.5°$. If the angle becomes exactly 90° the space group symmetry is $Cmmm$, No. 65.

2. *Simulations using a doubled unit cell*

The variation of energy and stress under [100] tensile loading, calculated using the doubled unit cell rotated by 45° (see Fig. 3), is shown in Fig. 6. The structure remains tetragonal up to the stress maximum of $\sigma_{max}^{100} = 2.57$ GPa at a critical strain of $\epsilon_c^{100} = 0.08$. Within the monoclinic description, the lattice constants of the structure at stress maximum are $a = 5.71$ Å, $b = 8.89$ Å, $c = 2.85$ Å, and $\beta = 103.7°$, almost exactly coincident with the results found with the smaller supercell.

After passing through the stress maximum, beyond a strain of $\epsilon = 0.1$ the structure becomes orthorhombically distorted ($b_{SC} \neq c_{SC}$ in the plane perpendicular to the applied uniaxial load). This distortion corresponds to the shear deformation ($\alpha < 90°$) of the 16-atom cell found in case 1. The energy reaches a maximum at $\epsilon = 0.24$, the structure is coincident with that for the energy maximum reached with the smaller supercell, and within the monoclinic description MC1 we have $a = 5.99$ Å, $b = 7.76$ Å, $c = 3.04$ Å, and $\beta = 95.8°$. At larger strain of $\epsilon \sim 0.25$, a modest monoclinic distortion of the supercell sets in which disappears again at a strain of 0.34. A stress-free energy minimum (higher by about 11.8 meV than the undistorted G1 structure) is found at $\epsilon = 0.42$, with lattice constants in the MC1 setting $a = 6.49$ Å, $b = 6.48$ Å, $c = 3.30$ Å, and $\beta = 89.9°$. With $a = b$ and $\beta = 90°$ a cell doubled in the c direction corresponds to the tetragonal $L6_0$ structure. In their search for the optimal decoration of the (eventually distorted) bcc structure for the Ti_3Nb alloy, Lazar *et al.*[31] had found that an $L6_0$ structure is the energetically least favorable alternative, 11.4 meV/atom higher in energy than the cubic G1 structure and with relaxed lattice constants

of $a = b = 6.499$ Å and $c = 6.56$ A. However, the $L6_0$-type decoration of the lattice was found to be very important for the understanding of the martensitic phase transitions, because the $L6_0$ structure can be continuously deformed to the orthorhombic structure of the α'' phase, while the G1 structure cannot. This has very important consequences for the kinetics of the phase transformation.

Together we have found in simulations using different supercells that under uniaxial ⟨100⟩ tensile loading the Ti_3Nb alloy reaches along a tetragonal deformation path a stress maximum of $\sigma^{100}_{\max}$ between 2.45 GPa (simulations with the cubic G1 cell) and 2.57 GPa (simulations with a doubled cell rotated by 45° around the direction of the applied strain), at a strain of $\epsilon = 0.08$. In a simulation using a cell with a weakly broken symmetry at a slightly lower strain of $\epsilon = 0.06$ a shear instability against an orthorhombic distortion has been detected, limiting the ITS to 2.4 GPa. The stress maximum is not determined by a high-symmetry saddle-point structure, although at very large strains we have identified stress-free structures which have been found to play an important role in the martensitic transformations of this alloy. The ratio of tensile strength to tensile modulus, $\sigma^{100}_{\max}/E_{100} = 0.046$ is exceptionally low in comparison to the value of 0.08 found for normal bcc metals (Mo, Ta) and even much lower than the value of 0.11 calculated for Nb with a low tensile modulus. This shows that the low value of the ITS found in this gum metal approximant cannot be caused by a low shear constant alone.

B. ⟨110⟩ uniaxial loading

Because the G1 structure contains chains of Nb atoms oriented along a ⟨111⟩ direction, uniaxial tensile loading along different ⟨110⟩ directions will not yield identical results. Supercells appropriate for simulations of uniaxial tensile deformations along a ⟨110⟩ direction of the cubic cell are shown in Fig. 7. Evidently, for the type-1 supercell loading along [110] creates a linearly increasing tensile strain on the Nb-Nb chains in the $(\bar{1}10)$ plane containing the direction of the applied load. In contrast for the type-2 supercell loading along the $[1\bar{1}0]$ direction creates a compressive strain on the Nb-Nb chain in the plane perpendicular to the direction of the applied load. Both supercells contain 32 atoms; the lattice constants are $a_{SC} = b_{SC} = a_0 \times \sqrt{2}$, $c_{SC} = a_0$.

Figure 8 shows the energy strain and stress-strain relations calculated with both supercells and using two different k-point meshes. At first sight the energy increases monotonously up to a very large strain of $\epsilon = 0.5$; the stress shows a maximum of 25 GPa at $\epsilon = 0.42$. A closer inspection shows a slight inflection in the energy-strain curve and a local maximum in the stress at $\epsilon^{110}_c = 0.04$. To verify the existence of the stress maximum, the calculations have repeated with a very small strain increment of 0.005 and convergence with respect to the BZ sampling has been examined. The initial slope of the stress-strain curve corresponds to a tensile modulus of $E_{110} = 84.1$ GPa, in excellent agreement with the value of 83.2 GPa derived from the calculated elastic constants. The stress maximum leads to a theoretical tensile strength of $\sigma^{110}_{\max}(1) = 2.21$ GPa, $\sigma^{110}_{\max}(1)/E_{110} = 0.026$ for the type-1 supercell, and $\sigma^{110}_{\max}(2) = 2.76$ GPa, and $\sigma^{110}_{\max}(2)/E_{110} = 0.033$ for type 2. The difference between the two values of the ITS is a consequence

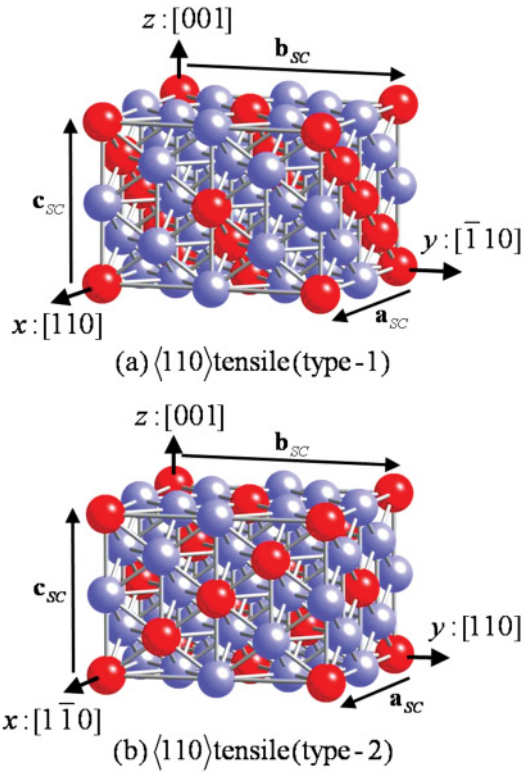

FIG. 7. (Color online) Supercells used to simulate ⟨110⟩ uniaxial tensile deformations of G1-type Ti_3Nb alloys. The strain is always applied along the x direction. Note the different orientations of the -Nb-Nb- chains relative to the direction of the applied load (cf. text).

of the different orientations of the -Nb-Nb- chains with respect to the direction of the applied tensile load. For a multidomain structure mixing different variants of the G1 structure, the ITS is given by the average of the two values, $\sigma^{110}_{\max} \sim 2.5$ GPa.

Thus, we have found two important results. (i) The ITS has the same almost equal extraordinarily low value of about 2.4 GPa for loading along the ⟨100⟩ and ⟨110⟩ directions. (ii) The ideal strength is the same, although the tensile modulus is much higher for the ⟨110⟩ direction. The ratio between ideal strength and tensile modulus is even lower for the ⟨110⟩ direction.

For both types of supercells the guiding symmetry along the deformation path under ⟨110⟩ tensile loading is monoclinic (see Fig. 9). With increasing strain (linearly increasing a_{SC}) the lattice is compressed along the c_{SC} direction (the [001] direction of the bcc lattice), while b_{SC} remains first unchanged and increases only on approaching the local stress maximum at $\epsilon^{110}_c = 0.04$. Both supercells undergo a very small monoclinic distortion counteracting the strain onto the Nb-Nb chains. For the type-1 supercell the angle β_{SC} increases beyond 90° such that the tensile strain on the -Nb-Nb- chains is reduced. For the type-2 supercell, the angle α_{SC} is reduced, reducing the compressive strain onto the Nb-Nb bonds in the plane perpendicular to the direction of the applied load.

At the first stress maximum small discontinuous changes of the lattice constants and the angle in the plane perpendicular to the applied load are observed. The crystal structure at the stress-maximum may be described by a MC1-type monoclinic

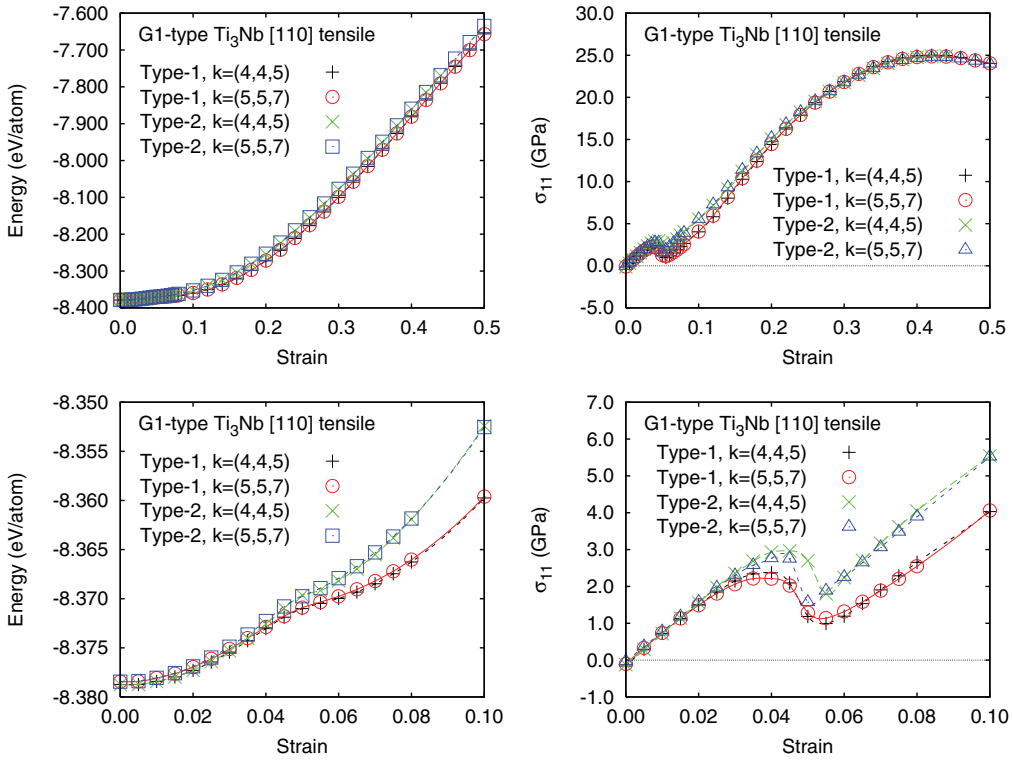

FIG. 8. (Color online) Variation of total energy (left panels) and stress (right panels) of G1-type Ti_3Nb as a function of the tensile strain along the [110] direction, calculated using two different supercells and different k-point meshes. The bottom panels show a zoom of the low-strain region (cf. text).

lattice with lattice constants $a = 5.73$ Å, $b = 9.29$ Å, $c = 2.87$ Å, $\beta = 113.6$ at $\epsilon = 0.04$ for type 1 and $a = 5.58$ Å, $b = 9.64$ Å, $c = 2.82$ Å, $\beta = 112.4$ at $\epsilon = 0.045$ for type 2.

V. RESPONSE TO SHEAR DEFORMATIONS

For the bcc metals V and Nb the saddle-point structure under $\{110\}\langle 111\rangle$ or $\{211\}\langle 111\rangle$ shear deformations is a special

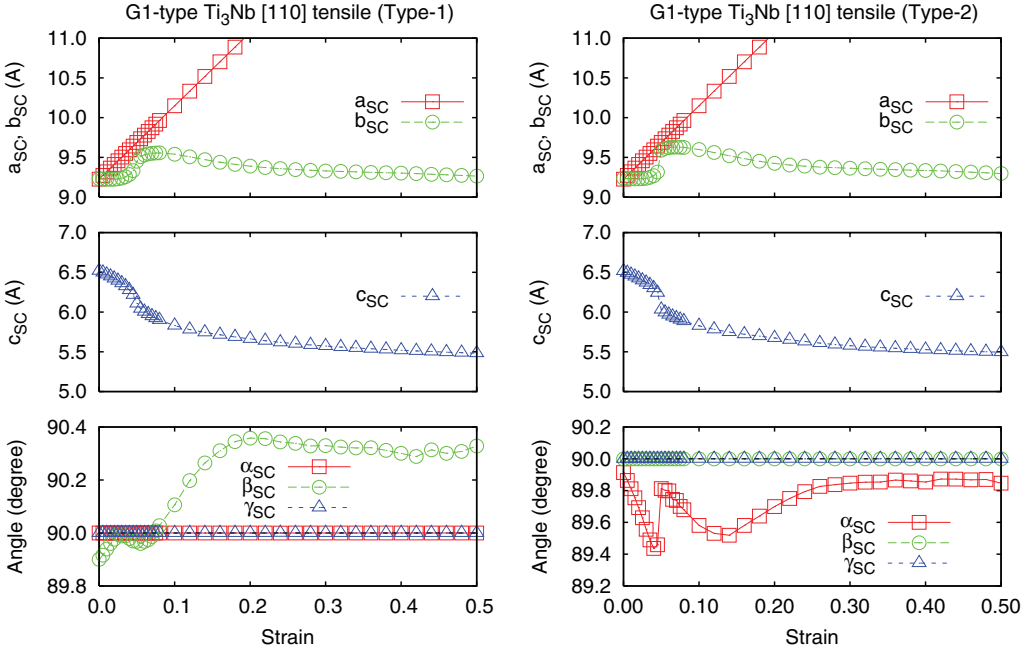

FIG. 9. (Color online) Variation of the lattice constants of type-1 and type-2 supercells used for the simulations of the response of G1-type Ti_3Nb to uniaxial tensile strain along a $\langle 110\rangle$ direction (cf. text).

body-centered tetragonal (bct) structure which is identical to the saddle-point structure reached after a bifurcation from the tetragonal to the orthorhombic deformation path under ⟨100⟩ uniaxial loading. Because the ITS is about twice as large as the ideal shear strength, both metals will fail by shear even under strictly uniaxial tensile loading. This stands in contrast to the normal bcc metals such as Mo or W, where the stress maximum under tensile loading is reached along a tetragonal deformation path and which fail by cleavage. The stress-strain curves of both classes of metals are also very different, those of V and Nb are very asymmetric, leading to an ideal shear strength which is much higher than expected on the basis of their low shear moduli.[15]

Gum metal alloys also fail under shear, but it was found that the scenario determining the behavior of V and Nb metals cannot be extended to gum metal. The VCA calculations of Li *et al.*[25] predicted that V-rich Ti-V alloys show the same behavior as V metal, but in alloys with less than 45 at.% V a shear instability is reached only at strains beyond the stress maximum under tension. Also, because in the VCA the alloys are treated as effective one-component systems with bcc symmetry, the saddle-point structures determining the ideal strength are determined by symmetry. Our results for G1-type Ti_3Nb alloys presented in the foregoing sections have demonstrated that this is not the case for real alloys, because as a consequence of the occupation of the lattice sites by different atomic species the symmetry of the deformed crystal is further reduced. Under tensile loading along the ⟨100⟩ and ⟨110⟩ directions the structure at the stress maximum can be described by the same monoclinic structure, which is not determined by any stress-free structure with higher symmetry. Failure by shear under uniaxial tensile loading requires that the same structure is also reached the stress maximum under shear and that the ideal shear strength is lower than the ITS.

We have considered the {211}⟨111⟩ and {110}⟨110⟩ shear systems. The first is the weakest slip system of the bcc metals; for the alloy it is also relevant for the transformation from the β to the ω phase.[31] The second is relevant in relation to a possible strain-induced transformation from the β to the α'' martensite. The information on the lattice constants of all supercells and the BZ meshes used in the calculations is compiled in Table III.

A. {211}⟨111⟩ shear deformation

Figure 10 shows the two computational cells containing 24 and 48 atoms respectively used for simulating shear deformations in a ⟨111⟩ direction on a {211} plane. The undeformed cells are orthorhombic, with lattice parameters a_{SC}, b_{SC}, and c_{SC} as defined in the figure and in Table III. The two supercells differ in the orientation of the shearing direction relative to the -Nb-Nb- chains. For type-1 supercells shearing occurs along the Nb-chains, for type-2 supercells the shearing direction is oblique to the orientation of the -Nb-Nb chains. As demonstrated below, this leads to slightly different results for the two supercells of different size.

The shear deformations have been performed in an alias mode;[29,30,48] that is, the strain is applied to the top layer of the supercell, while the bottom layer is kept in a fixed position and all intermediate layers are free to relax. The alias regime provides a more realistic description of a shear deformation than an affine transformation applied to all coordinates in the cell. The alias regime also allows the formation of stacking faults such that the competition between theoretical shear strength and stacking fault formation can be discussed on a common footing. For example, simulations of $\{\bar{1}10\}\langle 111\rangle$ and $\{11\bar{2}\}\langle 111\rangle$ shear deformations of face-centered cubic (fcc) Al have demonstrated that for both shear systems the ideal shear strength is limited by stacking fault formation, whereas for fcc Cu stacking fault formation occurs only at strains larger than the critical strain at the shear stress maximum.[48] For $\{\bar{1}10\}\langle 111\rangle$ shearing the microscopic analysis of the deformation mechanism permitted by the alias regime shows that the smallest possible perfect $\frac{1}{2}[\bar{1}10]$ dislocation is split into two partial Shockley dislocations $\frac{1}{6}[\bar{2}11] + \frac{1}{6}[\bar{1}2\bar{1}]$ because a stacking fault leads to a lower misfit energy. To perform the simulations in the alias regime is particularly important for gum metal approximants which are characterized by elastic deformations up to the ideal strength.[11,12]

Upon shearing a bcc lattice parallel to a {211} plane a mirrored bcc lattice is created at a strain of $\gamma = \sqrt{2}/2 \sim 0.71$ (the "twining" strain) if relaxation is excluded. If only a single maximum in the total energy exists for strains from 0 to 0.71, symmetry dictates that it must be located at $\gamma \sim 0.35$, and the inflection point must fall around 0.17. Along this deformation path the symmetry changes from cubic to monoclinic and further to orthorhombic at the saddle point. For an alloy, the symmetry can be further reduced by the chemical decoration of the bcc lattice.

The energy-strain and stress-strain curves for $\{211\}\langle 111\rangle$ sheared Ti_3Nb calculated with both types of supercells are shown in Fig. 11. With the type-1 supercell the initial slope of the stress-strain curve yields a shear modulus of $G_{111} = 24.9$ GPa, in good agreement with the value derived from the elastic constants ($G_{111} = 22.4$ GPa; see Table I). The ideal shear strength (ISS) is $\tau_{max}^{111} = 1.7$ GPa at a critical strain of $\gamma_c^{111} = 0.12$. A stress-free saddle-point structure is found at a strain of $\gamma \sim 0.34$.

At the stress maximum the structure can be described as monoclinic, with lattice parameters $a = 5.57(5.70)$ Å, $b = 9.08(8.89)$ Å, $c = 2.83(2.85)$ Å, and $\beta = 102.8(103.7)^\circ$, space group $C2/m$ in the MC1 setting. This structure is very similar to that reached at the stress maximum along the tetragonal deformation path under [100] tension whose lattice parameters are given in parentheses. The stress-free structure reached at a strain of $\gamma = 0.34$ is base-centered orthorhombic with lattice parameters $a = 5.61$ Å, $b = 8.94$ Å, $c = 2.81$ Å and space group $Cmmm$. This stress-free structure is determined by symmetry. Shearing along [111] changes the angle β of the MC1-type monoclinic cell, from the tetrahedral angle $\beta = 109.5^\circ$ for the unstrained G1 structure to 102.8° at the stress maximum and 90° at the energy maximum which 32 meV/atom higher than the G1 structure.

This structure has the same symmetry and is energetically nearly degenerate with the orthorhombic structure found under [100] uniaxial tension, if the angle α of the cubic cell of the G1 structure is fixed at 90° (case 3). The structure is also similar to that found at the energy minimum under unconstrained [100] uniaxial tension applied to the doubled unit cell, at $\epsilon^{100} = 0.42$, at an energy of 12 meV/atom above the ground-state structure.

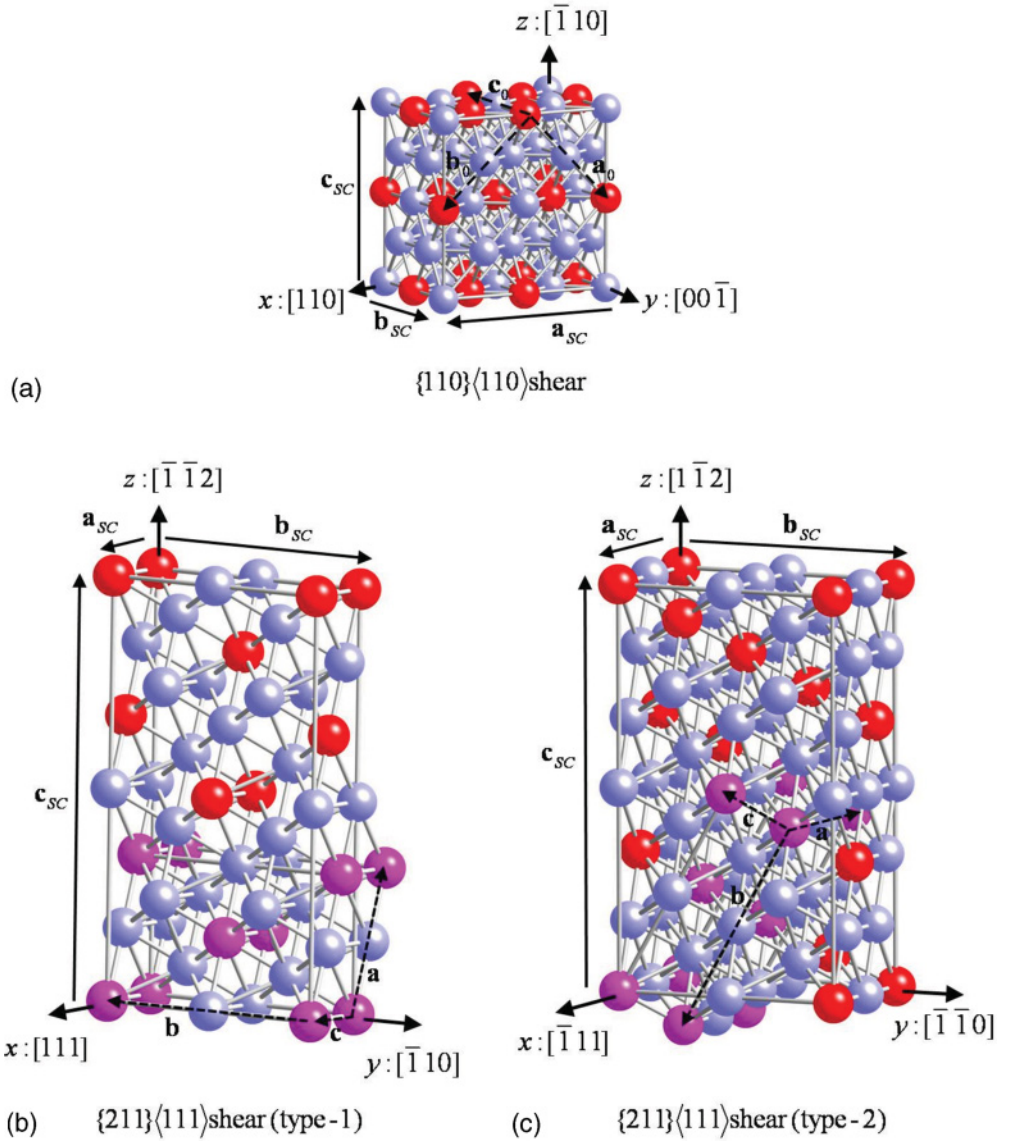

FIG. 10. (Color online) Supercells used to simulate {110}⟨110⟩ (a) and {211}⟨111⟩ (b),(c) shear deformations. In (a) the cubic unit cell of the G1 structure is indicated by the broken arrows; in (b) and (c) the smaller MC1-type monoclinic unit cell of the G1 structure has been emphasized (cf. Table III and text).

The three orthorhombic energy extrema differ, however, in the lattice constants.

Calculations using the larger type-2 supercell differ from those with the smaller type-1 cell by the absence of symmetry constraints. The type-1 supercell remains always monoclinic, while for a type-2 supercell a symmetry-breaking leading to triclinic symmetry is not excluded. Results are in almost perfect agreement with those described above up to a strain

TABLE III. Supercells used for the simulations of the response to shear loading (cf. text).

	Shear		
	{110}⟨110⟩	{211}⟨111⟩	
		Type 1	Type 2
x axis	$[110], a_{SC} = \sqrt{2} \times a_0$	$[111], a_{SC} = \frac{\sqrt{3}}{4} \times a_0$	$[\bar{1}11], a_{SC} = \frac{\sqrt{3}}{2} \times a_0$
y axis	$[001], b_{SC} = a_0$	$[\bar{1}10], b_{SC} = \sqrt{2} \times a_0$	$[\bar{1}\bar{1}0], b_{SC} = \sqrt{2} \times a_0$
z axis	$[\bar{1}10], c_{SC} = \sqrt{2} \times a_0$	$[\bar{1}\bar{1}2], c_{SC} = \sqrt{6} \times a_0$	$[1\bar{1}2], c_{SC} = \sqrt{6} \times a_0$
k mesh	$5 \times 7 \times 5$	$14 \times 5 \times 3$	$7 \times 5 \times 3$
N_{atoms}	32	24	48

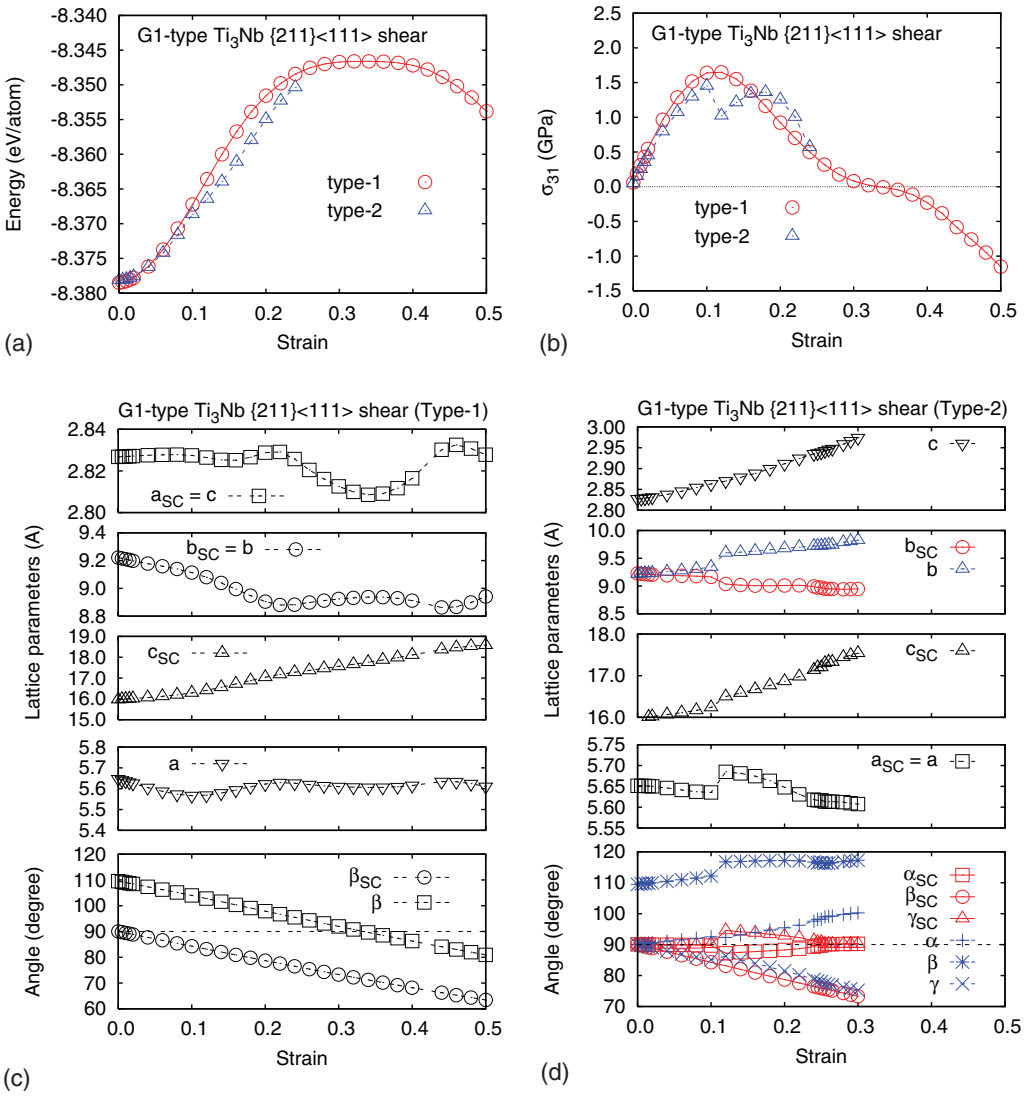

FIG. 11. (Color online) Variation of the total energy (a), the stress (b), the lattice constants and angles of the type-1 (c) and type-2 (d) supercells calculated for G1-type Ti_3Nb as a function of the applied strain under $\{211\}\langle 111\rangle$ shear deformations (cf. text).

of $\epsilon = 0.10$. At this strain the cell suddenly relaxes to a triclinic symmetry, the change in the angles is related to a discontinuous change in the lattice parameters a_{SC} and b_{SC}. The lattice parameters (in a framework derived from the MC1 structure) are $a = 5.64$ Å, $b = 9.34$ Å, $c = 2.86$ Å, $\alpha = 92.5°$, $\beta = 112.2°$, $\gamma = 85.1°$.

The stress maximum of $\tau_{max}^{111} = 1.5$ GPa and $\gamma_c^{111} = 0.10$ reached at the shear instability limits the ISS. At larger strains the deviations of the angles α_{SC} and γ_{SC} from 90° gradually decrease and also the lattice parameters a_{SC} and b_{SC} converge to the values calculated at the energy maximum with a type-1 supercell. Note that even for a type-1 supercell the energy-maximum of the saddle-point configuration is very flat, indicating the possibility of coexisting almost degenerate stress-free configurations. However, the differences between both sets of simulations are relevant only for plastic deformations beyond elastic failure, not for the determination of the ISS.

A real Ti_3Nb crystal will consist of domains representing different realizations of the G1 structure, with different orientations of the -Nb-Nb- chains relative to the shearing direction. The type-1 and type-2 supercells describe two such possible configurations. The important point is that for both we find values of the ISS which are considerably lower than the ITS under $\langle 100\rangle$ loading, and similar structures at the stress maximum. Hence, our simulations lead to the conclusion that even under strictly uniaxial tensile loading the alloy will fail by shear and not by cleavage, as found experimentally for gum metal alloys.

The dimensionless ISS is $\tau_{max}^{111}/G_{111} = 0.067$; this value is much lower than the exceptionally high dimensionless ISS calculated for bcc V and Nb metals of 0.17 (V) or 0.19 (Nb) due to a low shear modulus of $G_{111} = 33(31)$ GPa in combination with a modest ISS of $\tau_{max} = 5.5(6.0)$ GPa for V(Nb) and also significantly lower than the dimensionless ISS of $\tau_{max}/G_{111} = 0.11$–$0.12$ determined for "normal" bcc metals such as Mo, W, and Ta[15]. Hence, the low ISS of Ti_3Nb cannot be explained by a low value of the elastic modulus alone. Comparing the stress-strain curves of the bcc metals under shear with that of the G1-type Ti_3Nb alloys we find that the exceptional behavior of the alloy (which justifies its use as a "gum metal

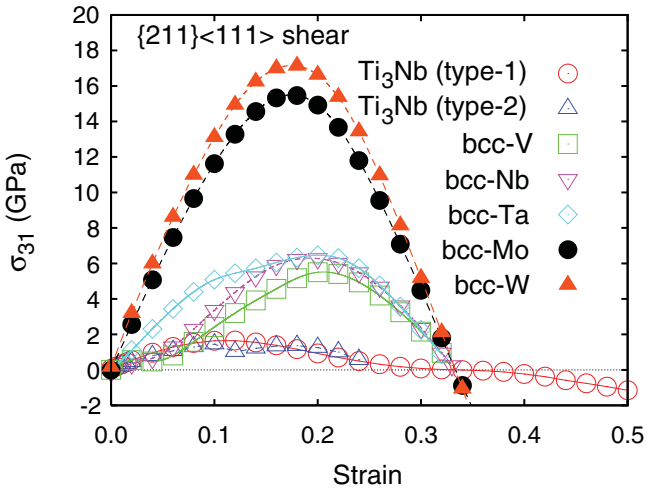

FIG. 12. (Color online) Comparison of the stress-strain curves of bcc V, Nb, Ta, Mo, and W with the G1-type Ti_3Nb alloy under $\{211\}\langle 111\rangle$ shear deformations.

approximant") is that it combines a low value of the shear modulus (as found also for V and Nb) with a rather "normal" stress-strain curve (as in Mo, W, and Ta); this is illustrated in Fig. 12. For V and Nb with a very low value of G_{111} and C_{44}, the stress-strain curve shows upward curvature at low strain; that is, the initially very soft lattice stiffens under increasing strain. It has been demonstrated[15] that at strains larger than about 0.08 in pure V and Nb a pure shear deformation is insufficient to relax all lateral stresses and that upon further deformation a volume expansion reflected by a nonmonotonous variation of the lattice constants under strain takes place. For Ti_3Nb we find that under shear a_{SC} remains almost constant, while b_{SC} decreases and c_{SC} increases monotonously up to strains well beyond the critical strain, the atomic volume remains constant. This means that the alloy remains soft also under strain and this is instrumental for achieving a low shear strength.

It is also remarkable that all stress-strain curves display a stress-free structure at $\gamma \sim 0.34$ which is determined by symmetry for both the bcc metals and the G1-type Ti_3Nb alloy. For the bcc metals the stress-free structure corresponds to the energy maximum separating the unstrained bcc structure and the mirrored bcc structure at $\gamma \sim 0.71$ for the G1-type compound to the base-centered orthorhombic structure realized if the angle β of the MC1-type monocinic cell reaches a value of 90° under shear.

B. $\{110\}\langle 110\rangle$ shear deformation

A (110)[110] shear deformation is of interest because this type of transformation is thought to be associated with the $\beta \rightarrow \alpha''$ transformation. The supercell containing 32 atoms (doubled unit cell) used for the simulation of this type of shear loading is shown in Fig. 10. The energy-strain and stress-

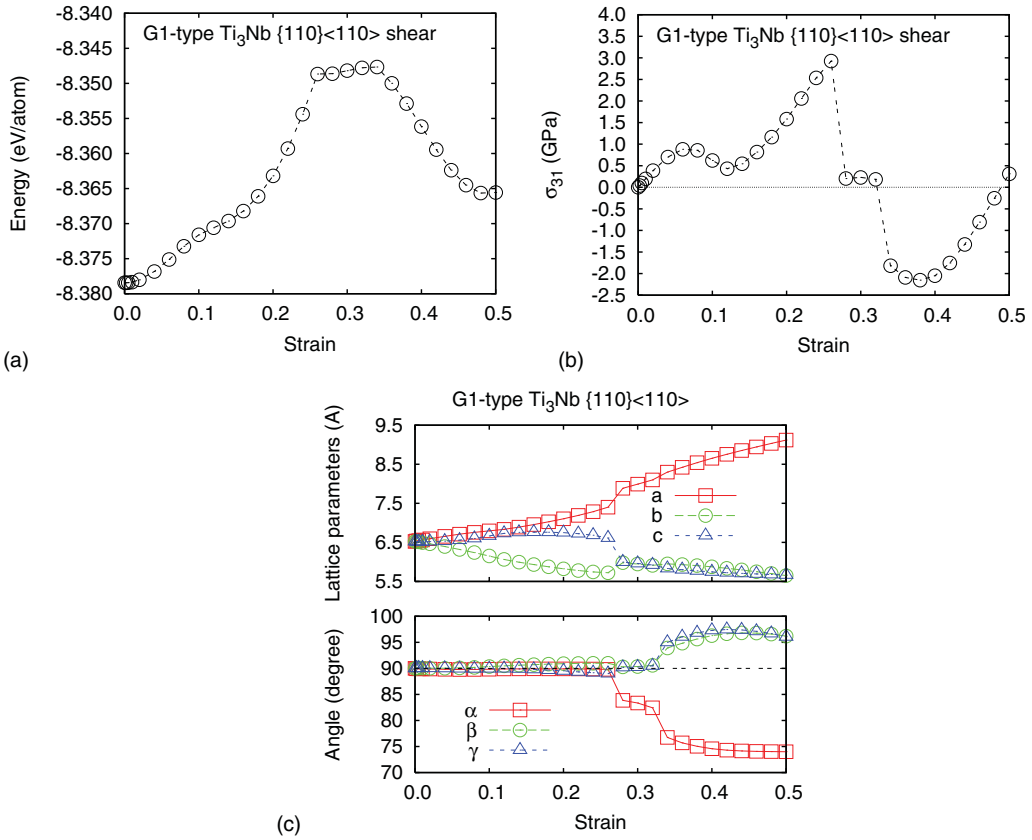

FIG. 13. (Color online) Variation of the total energy (a), the stress (b), the lattice constants and angles of the elementary cell (c) for G1-type Ti_3Nb as a function of the applied strain under $\{110\}\langle 110\rangle$ shear deformations.

strain curves are shown in Fig. 13. The initial slope of the stress-strain curve corresponds to a shear modulus of $G_{110} = 19.7$ GPa, in good agreement with the value of 18.7 GPa derived from the elastic constants. At a strain of $\gamma_c^{110} \sim 0.06$ a local stress maximum of $\tau_{\max}^{110} = 0.9$ GPa determining the ISS under $\{110\}\langle 110\rangle$ deformation is detected, although the stress increases again for larger strains until $\gamma \sim 0.26$, where the structure collapses to a stress-free configuration of higher energy. The dimensionless ISS is $\tau_{\max}^{110}/G_{110} = 0.048$.

Under increasing strain the lattice undergoes a series of transformations: Up to $\gamma^{110} = 0.26$ the supercell undergoes only a monoclinic deformation, with only modest changes in the lattice constants. This deformation of the supercell corresponds to an orthorhombic deformation of the cubic unit cell of the G1 structure [see Fig. 13(c)]. At larger strains beyond 0.26 the distortion of the supercell is triclinic; the crystal structure is monoclinic at strains between 0.26 and 0.34 and also triclinic beyond [see Fig. 13]. The crystal structure can also be described as a deformed MC1 unit cell, this permits the comparison with other deformation-induced structures. The structure at the first stress maximum is triclinic, with lattice parameters (in a framework derived from the MC1 structure) are $a = 5.64$ Å, $b = 9.22$ Å, $c = 2.83$ Å, $\alpha = 87.3^\circ$, $\beta = 109.1^\circ$, $\gamma = 92.8^\circ$. Evidently, this structure is very similar to that reached for type-2 (211)[111] shear deformation immediately after the first shear instability. At a large strain of $\gamma^{110} \sim 0.48$ a local energy minimum, about 13 meV/atom above the undistorted G1 structure is found. Within the MC1 setting the lattice parameters are $a = 5.93$ Å, $b = 6.85$ Å, $c = 3.42$ Å, $\alpha = 89.8^\circ$, $\beta = 89.7^\circ$, $\gamma = 89.9^\circ$; that is, within the computational accuracy the structure is orthorhombic. It is related to the stress-free $L6_0$ structure realized under $\langle 100\rangle$ tension through a compression of the lattice parameter a and an expansion of b and c, but energetically almost degenerate.

VI. DISCUSSION AND CONCLUSIONS

We have performed extensive *ab initio* DFT calculations of the response of β-phase Ti_3Nb alloys to tensile and shear loading, using different computational supercells to account for the influence of different possible orientations of the -Nb-Nb- chains characteristic for the ground-state G1-type ordering on the basic bcc lattice. A realistic β-phase structure will consist of domains with such different orientations of the -Nb-Nb- chains. Our results for the ideal tensile and shear strengths are compiled in Table IV.

TABLE IV. Ideal tensile and shear strengths $\sigma_{\max}$ and $\tau_{\max}$ (in GPa), critical strains ϵ_c and γ_c, and dimensionless tensile and shear strengths of Ti_3Nb for different loading conditions.

Uniaxial tension			
Direction	ϵ_c	$\sigma_{\max}$	$\sigma_{\max}/E$
$\langle 100\rangle$	0.06	2.4	0.046
$\langle 110\rangle$	0.04	2.5	0.026
Shear deformation			
Shear system	γ_c	$\tau_{\max}$	$\tau_{\max}/G$
$\{211\}\langle 111\rangle$	0.10	1.50	0.067
$\{110\}\langle 110\rangle$	0.06	0.90	0.048

Under uniaxial $\langle 100\rangle$ tensile strain a stress maximum of 2.45 GPa is found at a strain of $\epsilon^{100} = 0.08$ along a deformation path describing a tetragonal distortion of the supercell. However, a shear instability related to $C_{11} = C_{12}$ and $C_{22} = C_{23}$ leading to an orthorhombic distortion of the supercell is found at a slightly lower critical strain of $\epsilon_c^{100} = 0.06$, limiting the ITS to $\sigma_{\max}^{100} = 2.40$ GPa. The results are confirmed by calculations using a larger supercell. The shear instability limiting the tensile strength is rather weak; it may be bypassed if the strains are increased in the simulations by a too-large increment. The guiding crystalline symmetry under strain is monoclinic, for the structure at the stress maximum both supercells lead to identical results. Calculations with the larger supercell provide evidence for the existence of a stress-free energy minimum structure at a large strain of $\epsilon^{100} = 0.42$ which is just the tetragonal $L6_0$ structure found after relaxation of the bcc lattice with the chemical decoration leading to the highest energy.

Simulations of the response to uniaxial $\langle 110\rangle$ tension have been performed for two large supercells differing in the orientation of the -Nb-Nb- chains relative to the direction of the applied load. The ITS is determined by a premaximum of the stress at a critical strain of $\epsilon_c^{110} = 0.04$ (0.045) using type-1 (type-2) supercells and slightly different values of the ITS of $\sigma_{\max}^{110} = 2.21(2.76)$ GPa. Beyond the stress minimum around a strain of about 0.05, the stress increases monotonically to much larger values; the form of the stress-strain curve is similar to that reported by Li *et al.*[27,28] for B2-type FeAl compounds. The structures reached at the stress maxima are monoclinic, they are similar, but not identical to those at the critical stress under $\langle 100\rangle$ loading. The ideal strength of a multidomain sample displaying different orientations of the -Nb-Nb- chains may be approximated by the average over the results for monodomain crystals, $\sigma_{\max}^{110} \sim 2.5$ GPa.

The simulations of shear deformations have been performed in the alias mode and for large supercells. The simulations permit the formation of stacking faults, but this is not observed in any of the simulations. Hence, our results demonstrate that the ISS of this gum metal approximant is not limited by stacking fault formation.

The results show that the ITS is almost isotropic, in contrast to a negative shear anisotropy of $A = 2 \times (C' - C_{44})/C_{44} = -1.002$. The dimensionless ITSs are much lower than the values calculated for all bcc metals. The stress-strain curve of Ti_3Nb is fundamentally different from that of all bcc metals, where it is symmetry-dictated. Along the tetragonal deformation path of bcc metals under $\langle 100\rangle$ tension the saddle-point structure at the stress maximum is fcc, it determines the ITS of metals such as Mo or W. If the shear constant C_{44} (in a body-centered tetragonal reference frame) vanishes already before reaching the stress-maximum, a bifurcation to an orthorhombic deformation path takes place and limits the ITS to lower value for V and Nb. For Ta the bifurcation point coincides with the stress maximum along the tetragonal deformation path. The Ti_3Nb alloy has a negative shear anisotropy (like Ta), whereas V and Nb metals have a large

positive value of the anisotropy, $A = 4.4(4.9)$ (Ref. 15; note that the theoretical values are somewhat too large, but agree with experiment in the positive sign). The instability of Ti_3Nb on the primary tetragonal deformation path is determined by the conditions $C_{11} = C_{12}$ and $C_{22} = C_{23}$ (again in a body-centered tetragonal reference structure); this is different from the condition determining the bifurcation from the tetragonal to the orthorhombic deformation path for the pure metals. The bifurcation found for the bcc metals also leads to a continuous variation of energy and strain, whereas for the alloy we have found a discontinuous collapse of the strain to lower values (see Fig. 4). One must also remember that the tetragonal to orthorhombic deformation describes the change in the shape of the computational supercell, whereas the smallest possible unit cell describing the crystalline structure of the alloy subject to tensile strain is monoclinic.

Shear deformations following the $\{211\}\langle 111\rangle$ slip system have been simulated using two supercells differing in size and in the orientation of the -Nb-Nb- chains relative to the shearing direction (parallel for type 1, oblique for type 2). In both cases the supercell undergoes a monoclinic deformation. For the type-1 supercell the stress increases monotonously until a maximum of $\tau_{\max}^{111} = 1.7$ GPa at a shear strain of $\gamma^{111} \sim 0.12$. The type-2 supercell becomes instable against a triclinic deformation at a critical strain of $\gamma_c^{111} = 0.10$, limiting the ideal shear strength to $\tau^{111} = 1.5$ GPa. The important point is that the crystal structure at the stress maximum along the monoclinic deformation path is identical to that reached at the stress maximum under $\langle 100\rangle$ uniaxial loading. Since the ISS is much lower than the ITS, this means that even under purely uniaxial loading Ti_3Nb will fail by shear and not by cleavage.

The ISS of Ti_3Nb for shearing along a $\langle 111\rangle$ direction is lower by a factor of about four than that calculated for bcc V and Nb. The difference is slightly smaller for the dimensionless ISS because the shear modulus G_{111} alloy is lower for the alloy. The ratio the ideal shear and tensile strengths is $\tau^{111}/\sigma^{100} = 0.61, 0.47, 0.48$ for Ti_3Nb, V and Nb, respectively; it follows roughly the trend in the ratio in the shear and tensile moduli, $G_{111}/E_{100} = 0.42, 0.20, 0.21$. For the pure metals the body-centered tetragonal saddle-point structure at a shear strain of $\gamma \sim 0.35$ is dictated by symmetry; the guiding symmetry along the deformation path is monoclinic. For the Ti_3Nb alloy both the supercell and the crystal structure are monoclinic along the deformation path; the stress-free structure at the energy maximum (at $\gamma \sim 0.34$) the crystal structure is orthorhombic. The stress-free structure is similar, but not identical to that found under $\langle 100\rangle$ tension.

The response to $\{110\}\langle 110\rangle$ shear loading is similar to that to $\langle 110\rangle$ tension. The low ISS of $\tau_{\max}^{110} = 0.9$ GPa at $\gamma_c^{110} = 0.06$ is determined by a local maximum of the stress-strain curve. For larger strain the stress continues to increase to much larger values. Along the deformation path the shape of the supercell is monoclinic, the lattice constants undergo only very small changes. The guiding crystalline symmetry, however, is triclinic. At a strain of $\tau^{110} \sim 0.48$ the triclinic structure converges to an orthorhombic stress-free lattice. The stress-free structure found under very large tensile strain and for the two different shear systems are all three orthorhombic. They differ in the lattice constants, but all have almost the same atomic volume than the unstrained G1 structure.

It is interesting to correlate the results of our *ab initio* calculations to experimental measurements of the mechanical properties of alloys of similar compositions. Kim *et al.*[2,49] have performed tensile tests on binary Ti-Nb alloys with 22 to 28 at.%. Nb plus 0 to 2 at.% oxygen. The samples were polycrystalline and subject to cold working and annealing. The stress-strain curves showed a maximum stress of about 0.7 GPa in oxygen-free samples containing about 22 at.% Nb; addition of oxygen leads to an increase of the tensile strength to up to 1.35 GPa.

Furuta *et al.*[10,50] investigated polycrystalline samples of quaternary gum metal alloys containing Nb, Ta, Zr and a small percentage of oxygen. For an alloy containing 23 at.% of Nb the tensile strength is 1.37 GPa at a maximum elongation of 12%, for an alloy with a slightly higher Nb content the tensile strength increases to 1.5 GPa; the maximum elongation decreases to 10%. Other results on gum metal alloys have been compiled in the Introduction.[20,22–24,32] The results demonstrate that the tensile strength varies strongly with oxygen content, processing conditions, and temperature, between 0.4 GPa and 1.8 GPa. The shear strength for shearing in the $\langle 111\rangle$ direction has been estimated from nanoscopic compression experiments, leading to an average value of 0.85 GPa and a maximum of 1.8 GPa, depending on the pretreatment of the samples.

The important conclusion from our investigations is that we find for the β-phase Ti_3Nb alloy values of the ideal tensile and shear strengths which are much lower than those estimated before from the measured elastic constants,[32] due to stress-strain curves which are quite different from the sinusoidal shape assumed in the derivation of the semiempirical relations. Also the ITS is predicted to be quite isotropic, in contrast to the elastic tensile moduli. The value of the ITS of about 2.5 GPa calculated from the binary alloy approaches that of real gum metal specimens. The ISS is found to be more anisotropic, varying between between 0.9 and 1.5 GPa; again this is much lower than expected on the the basis of the elastic constants and the semiempirical relations. For shearing in the [111] the calculated value is at the upper limit of the values found in experiments on gum metal. Together with our previous work on martensitic transformations the present results on the ideal tensile and shear strength demonstrate that *ab initio* DFT provides an accurate description of the structural, elastic, and mechanical properties of these complex alloys and provide an atomistic insight on the deformation mechanisms.

ACKNOWLEDGMENTS

Work at the University of Vienna has been performed within the framework of the Special Research Program ViCoM (Vienna Computational Materials Laboratory) supported by the Austrian Science Funds (FWF) and through the cooperation with the Toyota Central Research and Development Laboratory. We thank T. Bučko for providing access to the GADGET structural optimization package.

*nagasako@mosk.tytlabs.co.jp
†rasahi@mosk.tytlabs.co.jp
‡juergen.hafner@univie.ac.at

[1]T. W. Duerig, J. Albrecht, D. Richter, and P. Fischer, Acta Metall. **30**, 2161 (1982).
[2]H. Y. Kim, S. Hashimoto, J. I. Kim, H. Hosoda, and S. Miyazaki, Mater. Trans. **45**, 2443 (2004).
[3]H. Hosoda, Y. Fukui, T. Inamura, K. Wakashima, S. Miyazaki, and K. Inoue, Mater. Sci. Forum **425–432**, 3121 (2003).
[4]T. Grosdidier and M. J. Philippe, Mater. Sci. Eng. A **291**, 218 (2000).
[5]P. J. S. Buenconsejo, H. Y. Kim, and S. Miyazaki, Acta Mater. **57**, 2509 (2009).
[6]C. A. Luke, R. Taggart, and D. H. Polonis, J. Nucl. Mater. **16**, 7 (1965).
[7]E. W. Collings and H. L. Gegel, Scr. Metall. **7**, 437 (1973).
[8]T. Saito, T. Furuta, J. H. Hwang, S. Kuramoto, K. Nishino, N. Suzuki, R. Chen, A. Yamada, K. Ito, Y. Seno, T. Nonaka, H. Ikehata, N. Nagasako, C. Iwamoto, Y. Ikuhara, and T. Sakuma, Science **300**, 464 (2003).
[9]H. Ikehata, N. Nagasako, T. Furuta, A. Fukumoto, K. Miwa, and T. Saito, Phys. Rev. B **70**, 174113 (2004).
[10]T. Furuta, S. Kuramoto, H. H. Hwang, K. Nishino, and T. Saito, Mater. Trans. **46**, 3001 (2005).
[11]S. Kuramoto, T. Furuta, J. H. Hwang, K. Nishino, and T. Saito, Metall. Mater. Trans. A **37**, 657 (2006).
[12]M. Y. Gudkin, T. Ishizaki, S. Kuramoto, and I. A. Ovidko, Acta Mater. **54**, 2489 (2006).
[13]D. Roundy, C. R. Krenn, M. L. Cohen, and J. W. Morris Jr., Phys. Rev. Lett. **82**, 2713 (1999).
[14]D. Roundy, C. R. Krenn, M. L. Cohen, and J. W. Morris Jr., Philos. Mag. A **81**, 1725 (2001).
[15]N. Nagasako, M. Jahnátek, R. Asahi, and J. Hafner, Phys. Rev. B **81**, 094108 (2010).
[16]S. Kuramoto, T. Furuta, J. Hwang, K. Nishino, and T. Saito, Mater. Sci. Eng. A **442**, 454 (2006).
[17]M. Yu. Gutkin, I. Ishizaki, S. Kuramoto, I. A. Ovdiko, and N. K. Skiba, Int. J. Plast. **24**, 1333 (2008).
[18]M. Kiritani, Mater. Sci. Eng. A **350**, 1 (2003).
[19]M. Komatsu, Y. Matsukawa, K. Yasunaga, and M. Kiritani, Mater. Sci. Eng. A **350**, 25 (2003).
[20]J. W. Morris Jr., Y. Hanlumyang, M. Sherburne, E. Withey, D. C. Chrzan, S. Kuramoto, Y. Hayashi, and M. Hara, Acta Mater. **58**, 3271 (2010).
[21]D. L. Moffat and D. C. Larbalestier, Metall. Trans. A **19**, 1677 (1988); **19**, 1687 (1988).
[22]E. A. Withey, A. M. Minor, D. C. Chrzan, J. W. Morris, and S. Kuramoto, Acta Mater. **58**, 2652 (2010).
[23]Y. Yang, G. P. Li, G. M. Cheng, H. Wang, M. Zhang, F. Xu, and K. Yang, Scr. Mater. **58**, 9 (2008).
[24]M. Besse, P. Castany, and T. Gloriant, Acta Mater. **59**, 5982 (2011).
[25]T. Li, J. W. Morris, N. Nagasako, S. Kuramoto, and D. C. Chrzan, Phys. Rev. Lett. **98**, 105503 (2007).
[26]M. Šob, L. G. Wan, and V. Vitek, Philos. Mag. B **78**, 653 (1998).
[27]T. Li, J. W. Morris, and D. C. Chrzan, Phys. Rev. B **70**, 054107 (2004).
[28]T. Li, J. W. Morris, and D. C. Chrzan, Phys. Rev. B **73**, 024105 (2006).
[29]M. Jahnátek, M. Krajčí, and J. Hafner, Phys. Rev. B **76**, 014110 (2007).
[30]M. Jahnátek, M. Krajčí, and J. Hafner, Philos. Mag. **91**, 491 (2011).
[31]P. Lazar, M. Jahnatek, J. Hafner, N. Nagasako, R. Asahi, C. Blaas-Schenner, M. Stohr, and R. Podloucky, Phys. Rev. B **84**, 054202 (2011).
[32]N. Takesue, N. Shimizu, T. Yano, M. Hara, and S. Kuramoto, J. Cryst. Growth **311**, 3319 (2009).
[33]R. J. Talling, R. J. Dashwood, M. Jackson, S. Kuramoto, and D. Dye, Scr. Mater. **59**, 669 (2008).
[34]R. J. Talling, R. J. Dashwood, M. Jackson, and D. Dye, Scr. Mater. **60**, 1000 (2009).
[35]W. Cochran and R. A. Cowley, *Handbuch der Physik* (Springer, Berlin, 1967).
[36]P. Souvatzis, O. Eriksson, M. I. Katsnelson, and S. P. Rudin, Phys. Rev. Lett. **1000**, 095901 (2008).
[37]G. Kresse and J. Furthmüller, Comput. Mater. Sci. **6**, 15 (1996).
[38]G. Kresse and J. Furthmüller, Phys. Rev. B **54**, 11169 (1996).
[39]J. P. Perdew, J. A. Chevary, S. H. Vosko, K. A. Jackson, M. R. Pederson, D. J. Singh, and C. Fiolhais, Phys. Rev. B **46**, 6671 (1992).
[40]P. E. Blöchl, Phys. Rev. B **50**, 17953 (1994).
[41]G. Kresse and D. Joubert, Phys. Rev. B **59**, 1758 (1999).
[42]T. Bučko, J. Hafner, and J. G. Ángyán, J. Chem. Phys. **122**, 124508 (2005).
[43]R. P. Feynman, Phys. Rev. **56**, 340 (1939).
[44]O. H. Nielsen and R. M. Martin, Phys. Rev. Lett. **50**, 697 (1983).
[45]H. J. Monkhorst and J. D. Pack, Phys. Rev. B **13**, 5188 (1976).
[46]M. Methfessel and A. T. Paxton, Phys. Rev. B **40**, 3616 (1989).
[47]R. Hill and F. Milstein, Phys. Rev. B **15**, 3087 (1977).
[48]M. Jahnatek, J. Hafner, and M. Krajci, Phys. Rev. B **79**, 224103 (2009).
[49]J. I. Kim, H. Y. Kim, K. Hosoda, and S. Miyazaki, Mater. Trans. **46**, 852 (2005).
[50]T. Furuta, S. Kuramoto, J. Hwang, K. Nishino, T. Saito, and M. Niinomi, Mater. Trans. **5**, 1124 (2007).